MASTERARBEIT | MASTER'S THESIS

Titel | Title

Comparative analysis of morphology, migration and drug response of cancer-associated fibroblasts from pleural mesothelioma patients with distinct clinical outcomes

verfasst von | submitted by

Oscar Wagner

angestrebter akademischer Grad | in partial fulfilment of the requirements for the degree of

Master of Science (MSc)

Wien | Vienna, 2026

Studienkennzahl lt. Studienblatt | Degree programme code as it appears on the student record sheet:	UA 066 830
Studienrichtung lt. Studienblatt | Degree programme as it appears on the student record sheet:	Masterstudium Molecular Microbiology, Microbial Ecology and Immunobiology
Betreut von | Supervisor:	Dr. Sebastian Carotta

Abstract (English)

Pleural mesothelioma is an aggressive malignancy characterised by poor prognosis and a highly complex tumour microenvironment. Cancer-associated fibroblasts (CAFs) represent a major stromal component and are known to contribute to tumour progression through extracellular matrix remodelling, mechanical regulation and modulation of tumour cell behaviour. However, the functional heterogeneity of CAFs derived from patients with distinct clinical outcomes remains insufficiently understood.

The present study aimed to comparatively analyse morphology, migratory behaviour and drug responsiveness of two CAF cell lines derived from pleural mesothelioma patients with distinct clinical outcomes. Meso125F cells originate from a patient with prolonged survival (1028 days after diagnosis), whereas VMC59F cells were derived from a patient with shorter survival (420 days after diagnosis). Quantitative live cell imaging was performed to assess cell area, aspect ratio, circularity, migration speed and persistence.

Additionally, cytoskeletal organisation was evaluated by immunofluorescence staining of vimentin, α-tubulin and actin followed by coherency analysis using the OrientationJ plugin in Fiji. The effects of the vimentin-targeting compound ALD-R491 were investigated with respect to cell viability, morphology and cytoskeletal organisation. Furthermore, the response to transforming growth factor-β type 1 (TGF-β1) stimulation was examined descriptively.

The two CAF cell lines displayed distinct phenotypic characteristics. Meso125F cells exhibited significantly larger cell areas, whereas VMC59F cells showed markedly higher migration speed. While migration persistence did not differ significantly between the cell lines, only VMC59F cells demonstrated a positive correlation between migration speed and persistence, suggesting a more coordinated migratory phenotype.

ALD-R491 treatment did not impair cell viability and did not induce significant alterations in cytoskeletal coherency of vimentin, tubulin or actin. A modest reduction in cell area was observed following ALD-R491 treatment, without pronounced changes in overall cell shape. TGF-β1 stimulation resulted in progressive cell growth over time, although the analysis was descriptive in nature.

In summary, this study demonstrates functional heterogeneity between different patient derived mesothelioma CAFs and identifies migration speed as a key distinguishing

parameter. Pharmacological targeting of vimentin did not induce major structural cytoskeletal reorganisation under the investigated conditions, suggesting that potential effects of ALD-R491 may be subtle or context-dependent. These findings highlight the importance of considering stromal diversity in the tumour microenvironment and provide a basis for further investigation of CAF-targeted therapeutic strategies.

Abstract (German)

Das Pleuramesotheliom ist eine aggressive bösartige Erkrankung, die durch eine schlechte Prognose und eine komplexe Tumormikroumgebung (TME) gekennzeichnet ist. Krebsassoziierte Fibroblasten (CAFs) stellen einen wesentlichen Bestandteil des Stromas dar und tragen durch die Umgestaltung der extrazellulären Matrix, mechanische Regulation sowie die Modulation des Tumorzellverhaltens zur Tumorprogression bei. Die funktionelle Heterogenität von CAFs aus Patienten mit unterschiedlichen klinischen Verläufen ist jedoch bislang unzureichend charakterisiert.

Ziel dieser Studie war es, Morphologie, Migrationsverhalten und Arzneimittelempfindlichkeit von zwei CAF-Zelllinien aus Pleuramesotheliom-Patienten mit unterschiedlichen Überlebensprognosen vergleichend zu analysieren. Meso125F-Zellen stammen von einem Patienten mit längerer Überlebenszeit (1028 Tage nach der Diagnose), während VMC59F-Zellen von einem Patienten mit kürzerer Überlebenszeit (420 Tage nach der Diagnose) gewonnen wurden. Hierzu wurde eine quantitative Live-Cell-Imaging-Analyse durchgeführt, um Zellfläche, Seitenverhältnis, Rundheit, Migrationsgeschwindigkeit und Persistenz zu bestimmen.

Ergänzend wurde die Zytoskelettorganisation mittels Immunfluoreszenzfärbung von Vimentin, α-Tubulin und Aktin untersucht und anschließend durch eine Kohärenzanalyse mit dem OrientationJ-Plugin in Fiji ausgewertet. Die Effekte der auf Vimentin abzielenden Verbindung ALD-R491 wurden hinsichtlich Zellviabilität, Morphologie und Zytoskelettorganisation analysiert. Darüber hinaus wurde die Reaktion auf eine Stimulation mit transformierendem Wachstumsfaktor-β Typ I (TGF-β1) deskriptiv untersucht.

Die beiden CAF-Zelllinien zeigten deutliche phänotypische Unterschiede. Meso125F-Zellen wiesen signifikant größere Zellflächen auf, während VMC59F-Zellen eine höhere Migrationsgeschwindigkeit zeigten. Die Migrationspersistenz unterschied sich nicht signifikant, jedoch zeigte nur VMC59F eine positive Korrelation zwischen Geschwindigkeit und Persistenz, was auf einen stärker koordinierten Migrationsphänotyp hindeutet.

Die Behandlung mit ALD-R491 beeinträchtigte die Zellviabilität nicht und führte zu keinen signifikanten Veränderungen der Zytoskelettkohärenz von Vimentin, Tubulin oder Aktin. Es wurde jedoch eine leichte Reduktion der Zellfläche ohne wesentliche Veränderung der Zellform beobachtet. Die TGF-β1 Stimulation führte zu einem zeitabhängigen Anstieg der Zellfläche, wobei die Analyse deskriptiv blieb.

Zusammenfassend verdeutlicht diese Studie die funktionelle Heterogenität von aus verschiedenen Patienten stammenden CAFs im Mesotheliom und identifiziert die Migrationsgeschwindigkeit als wichtigen Unterscheidungsparameter. Die pharmakologische Modulation von Vimentin führte unter den untersuchten Bedingungen zu keiner ausgeprägten strukturellen Umgestaltung des Zytoskeletts, was auf subtile oder kontextabhängige Effekte von ALD-R491 hindeutet. Diese Ergebnisse unterstreichen die Bedeutung der Stromavielfalt in der TME und liefern eine Grundlage für zukünftige CAF-gerichtete Therapieansätze.

Table of contents

List of figures

List of abbreviations

ATP – Adenosine triphosphate

α-SMA – α smooth muscle actin

BSA – Bovine serum albumin

CAF – Cancer-associated fibroblast

DAPI – 4′,6-diamidino-2-phenylindole

DMSO – Dimethyl sulfoxide

ECM – Extracellular matrix

EDTA – Ethylenediaminetetraacetic acid

FAP – Fibroblast activation protein

FBS – Foetal bovine serum

HEPES – 4-(2-hydroxyethyl)-1-piperazineethanesulfonic acid

H+L – Heavy and light chain

PBS – phosphate buffered saline

PM – Pleural mesothelioma

RLU – Relative light units

ROI – Region of interest

TGF-ß1 – Transforming growth factor ß type 1

TME – Tumour microenvironment

Introduction

Pleural mesothelioma: clinical and biological challenges

Pleural mesothelioma (PM) is an aggressive malignancy arising from mesothelial cells lining the pleura and is strongly associated with prior asbestos exposure [1,2]. Despite declining asbestos use in many countries, the long latency period between exposure and disease manifestation continues to result in a substantial global disease burden [3,4]. Although asbestos is recognised as the predominant cause, other contributing risk factors may involve inherited predisposition, exposure to radiation, and simian virus 40 infection [3,5]. PM is characterised by diffuse local invasion, resistance to therapy, and poor overall prognosis [2,6].

Histologically, PM is classified into epithelioid, biphasic, and sarcomatoid subtypes, with epithelioid tumours exhibiting comparatively better survival outcomes [2,7]. Molecularly, PM frequently harbours alterations in tumour suppressor genes [8] such as BAP1, CDKN2A, and NF2, while lacking the high mutational burden seen in many epithelial cancers [9,10]. This relative genomic stability suggests that non-genetic factors, including tumour–stroma interactions, may significantly contribute to disease progression. Despite multimodal treatment strategies comprising platinum-based chemotherapy, surgery, radiotherapy, and more recently immunotherapy, median overall survival remains limited [11,12]. These limitations underscore the need to better understand the tumour microenvironment (TME) and its contribution to disease aggressiveness.

The tumour microenvironment and the role of cancer-associated fibroblasts

The TME plays a central role in cancer progression and is characterised by complex interactions between tumour cells, stromal components, and immune cells [13,14]. In pleural mesothelioma, the TME is typically heterogeneous and predominantly immunosuppressive, with tumour-associated macrophages and dysfunctional tumour-infiltrating lymphocytes contributing to tumour progression and immune evasion [15,16]. Within this context, non-malignant stromal cells further shape tumour behaviour and therapeutic response [14,17]. Among stromal components, cancer-associated fibroblasts (CAFs) represent one of the most

abundant and functionally versatile cell types [18,19]. CAFs originate from resident fibroblasts, mesothelial cells, pericytes, or other precursor populations and undergo activation in response to tumour-derived signals such as transforming growth factor-β I (TGF-β1) and inflammatory mediators [18,20]. Once activated, CAFs contribute to extracellular matrix (ECM) remodelling, paracrine signalling, immune modulation and regulation of tumour cell invasion and metastasis [17,21]. Recent studies in pleural mesothelioma have demonstrated that mesothelioma-associated fibroblasts enhance tumour cell proliferation and migration through paracrine signalling pathways, including c-Met, PI3K, and WNT signalling axes [8]. These findings support the concept that CAFs are active drivers of tumour progression rather than passive structural components.

Importantly, CAF populations are highly heterogeneous and may differ in their functional properties depending on tumour context and patient-specific factors [20,22]. However, in pleural mesothelioma, comparative analyses of patient-derived CAF behaviour remain limited.

Cytoskeletal organisation as a determinant of CAF function

Fibroblasts are defined not only by their secretory activity but also by their distinct cytoskeletal architecture [23,24]. The cytoskeleton composed of actin filaments, microtubules, and intermediate filaments such as vimentin, governs cell morphology, mechanical stability, migration, and force generation [25,26].

Vimentin

Vimentin is a hallmark intermediate filament of mesenchymal cells and plays a key role in maintaining cell integrity, mechanical resilience, and migration [25,26]. Through its interaction with actin filaments and microtubules, vimentin modulates cytoskeletal dynamics and facilitates directed cell migration. [25,26]

Actin

Contractile forces in adherent cells arise from actomyosin interactions, where filamentous actin and non-muscle myosin II assemble into contractile structures such as stress fibers [26,27]. These forces are essential for focal adhesion maturation, traction generation, and persistent migration [28,29]. In activated fibroblasts, actin remodelling is closely associated with myofibroblast differentiation and increased ECM remodelling capacity [30,31].

Tubulin

Microtubules are made of α-tubulin and β-tubulin heterodimers and regulate cell polarity as well as directional persistence by coordinating vesicle trafficking and signalling cascades [26,32]. Crosstalk between microtubules and actin networks is critical for coordinated cell migration [28,33].

Despite the recognised importance of cytoskeletal organisation in fibroblast biology, little is known about how cytoskeletal architecture varies among patient-derived CAFs in pleural mesothelioma and whether such differences correlate with migratory behaviour or clinical outcome.

Cell migration dynamics: speed, persistence, and rear retraction

Cell migration is a tightly coordinated process involving protrusion, adhesion formation, contraction, and rear detachment [28,33]. Quantitative parameters such as mean migration speed and directional persistence are widely used to characterise migratory phenotypes [34,35]. Mesenchymal migration requires efficient trailing edge retraction, which depends on cytoskeletal contractility and adhesion turnover [28,33]. Impaired rear detachment can result in elongated cell morphologies and "tail-like" structures, whereas efficient detachment promotes faster migration [36,37]. The dynamic remodelling of the trailing edge sometimes culminating in complete "tail loss" reflects cytoskeletal tension release and adhesion disassembly [36,37]. While such phenomena have been described in migrating fibroblasts, their occurrence and biological implications in pleural mesothelioma CAFs have not been systematically analysed.

TGF-β1 signalling in fibroblast activation and growth regulation

TGF-β1 is a central mediator of fibroblast activation and myofibroblast differentiation [38,39]. TGF-β1 promotes cytoskeletal remodelling, actin stress fiber formation, ECM deposition and changes in proliferation dynamics [40,41]. In many tumour contexts, TGF-β1 enhances CAF activation and promotes tumour-supportive phenotypes [39,41]. However, its effects may vary depending on fibroblast subtype and context, potentially influencing growth characteristics and morphology [41,42]. Understanding how patient-derived

mesothelioma CAFs respond to TGF-β1 provides insight into their activation state and plasticity.

Targeting stromal components: rationale for ALD-R491 treatment

Therapeutic strategies in PM have primarily focused on tumour cells [43,44]. However, increasing evidence suggests that targeting stromal components may enhance treatment efficacy [45,46]. In this work ALD-R491 was investigated for potential effects on cell viability, morphological parameters and cytoskeletal organisation of mesothelioma-associated CAFs.

ALD-R491 is an orally bioavailable small-molecule compound that directly targets the intermediate filament protein vimentin and has been shown to regulate filament stability, cell contractile force, and migration dynamics without inducing cytotoxic filament collapse [47–49]. In preclinical models, ALD-R491 modulated mesenchymal cell behaviour, partially reversed epithelial-to-mesenchymal transition phenotypes, and exerted anti-inflammatory and host-protective effects [47–49]. By assessing cytoskeletal coherency of vimentin, actin, and tubulin networks following treatment, this study aims to determine whether pharmacological intervention alters structural organisation and functional properties of mesothelioma-associated CAFs.

Study rationale and objectives

This study performs a comparative analysis of two patient-derived pleural mesothelioma CAF cell lines:

- **VMC59F**, derived from a 78-year-old male patient treated with induction chemotherapy (cisplatin/pemetrexed) followed by surgery, with an overall survival of 420 days after diagnosis.
- **Meso125F**, derived from a 65-year-old male patient treated with trimodality therapy (carboplatin/pemetrexed induction chemotherapy, surgery, and radiotherapy), with a survival of 1028 days.

Both CAF lines originate from epithelioid pleural mesothelioma but are associated with markedly different clinical outcomes.

The central hypothesis of this work is that CAF morphology, migration dynamics, and cytoskeletal organisation differ between patients with distinct clinical courses. This may reflect functional heterogeneity within the TME and provide a foundation for future therapeutic approaches. To address this hypothesis, the focus of this work is on quantifying baseline morphological parameters (area, aspect ratio, circularity), analysing migration dynamics using live-cell imaging, including mean speed and persistence as well as investigating the impact of ALD-R491 on cell viability, morphology, and cytoskeletal organisation. By integrating morphological, migratory, and pharmacological analyses, this work aims to contribute to a deeper understanding of stromal heterogeneity in pleural mesothelioma and its potential relevance to disease progression.

Materials and Methods

Origin of pleural mesothelioma cancer-associated fibroblast

The CAF cell lines Meso125F and VMC59F originate from samples taken during surgical resections from PM patients at the Department of Thoracic Surgery of the Medical University of Vienna, Austria and were sent by Dr. Michael Grusch to the research group of Prof. Dr. Katalin Dobra of the Department of Oncology and Pathology Karolinska Institutet Stockholm, Sweden.

Both CAF cell lines were taken from epithelioid PM tissue. VMC59F CAFs were obtained from a male 78-year-old patient who was treated with induction chemotherapy with cisplatin/pemetrexed followed by surgical resection with a survival time of 420 days after the PM diagnosis. Meso125F CAFs were obtained from a male 65-year-old patient who was treated with trimodality therapy consisting of induction chemotherapy with carboplatin/pemetrexed, surgery, and postoperative radiotherapy and a survival time of 1028 days after the PM diagnosis.

Cell culture

Both CAF cell lines were thawed and cultured in T25 flasks (Thermo Scientific) using RPMI 1640 medium with L-glutamine (Gibco, Cat. No. 11875093) supplemented with 10% heat-inactivated foetal bovine serum (FBS), 1% penicillin–streptomycin, and 15 mM 4-(2-hydroxyethyl)-1-piperazineethanesulfonic acid (HEPES; Gibco, Cat. No. 15630106). The cells were incubated at 37° C and 5% CO_2. Unless stated otherwise, all references to "medium" in this study refer to this complete RPMI-based culture medium. Flasks with 80-100% confluency were split to a 50% confluency. For this the medium was removed, the cells then were washed with Dulbecco´s phosphate buffered saline (PBS) followed by trypsinisation with 1:10 PBS diluted 0.5% trypsin-ethylenediaminetetraacetic acid (EDTA; Gibco, Cat. No. 15400054) for approximately 4 min. After detaching, the trypsin was inactivated with medium, and the cell suspension was then split accordingly into fresh T25 flasks. The missing volume in each T25 flask was filled up with medium to a total of 4 ml.

Cell seeding for live cell imaging

For the live cell imaging experiment the cells were seeded into an 8-well chamber slide. The following seeding procedure was performed for the first live cell imaging experiment. First the cells were counted using a Bürker counting chamber after mixing the cell suspension 1:1 with 0.4% trypan blue solution (Gibco, Cat. No. 15250061) to assess cell viability, followed by loading of the mixture into the chamber for counting. For each cell line one well containing 2000 cells per well was prepared by applying the previously mentioned splitting steps.

For experiment Nr. 4 the cells were seeded based on their confluency in the T25 flask to reach a seeding confluency of 50% in each well. The missing volume in each well of the cell containing 8-well chamber slide was filled up with medium to a total of 500 µl. On the next day the medium was removed, the cells were washed with PBS and 500 µl mixture of 0.025 µg Hoechst (Invitrogen, Cat. No. H3570) staining and medium containing the same composition as the previously mentioned medium but without phenol red were added. The total concentration of Hoechst in each well was 0.05 µg/mL [49,50]. After the mixture was added the 8-well chamber slide was covered with aluminium foil and secured in a polystyrene box to insulate it and for prevention of light exposure before transferring it to the Zeiss CellObserver 7 microscope at the Biomedicum Imaging Core Facility of Karolinska Institutet.

Live cell imaging

Prior to image acquisition, the microscope was manually focused and each well of the 8-well chamber slide was centred using the system Zeiss Zen software (Zeiss, version 3.2). Time-lapse imaging was conducted over a total duration of 20 hours, with images acquired automatically every 40 minutes. Phase-contrast images were captured using a 20x objective. In addition, nuclear staining was recorded using a Hoechst filter set (excitation 405 nm / emission 486 nm) also using a 20x objective. All acquired images were saved as TIF files and used for subsequent digital image analysis.

Computational image analysis

Image analysis was performed using Fiji (ImageJ, version 1.54p).

Morphological analysis

Cell area, aspect ratio, and circularity were determined using the "Measure" function under the "Analyze" tab. Individual cells were manually outlined in the phase-contrast channel using the "Freehand Selection" tool prior to measurement. All morphological analyses were conducted using images from the first time point of the live cell imaging experiment to ensure consistent baseline comparison between cell lines.

Migration analysis

Mean speed and persistence were determined using the nuclear Hoechst channel and the Fiji tracking plugin *TrackMate*. For analysis, the field of view was subdivided into smaller regions using the "Crop" function. Background signal was reduced using the "Subtract Background" function (rolling ball algorithm, default settings). Cell tracking was performed using the thresholding detector in TrackMate. Threshold intensity and track quality parameters were determined using the automatic selection tools and verified manually. Automatically detected tracks were reviewed individually. Fragmented tracks belonging to the same cell were manually merged. Tracks not corresponding to actual cell migration events were excluded from analysis. All extracted parameters were compiled in result tables generated by Fiji and exported for further statistical evaluation.

Statistical analysis and data visualisation

Raw data obtained from Fiji were analysed using Prism (GraphPad, Prism 6).

For each parameter, values were entered into separate columns using the "Column" data table format. Normal distribution was assessed using the D'Agostino–Pearson omnibus normality test under "Column analyses". If both datasets passed the normality test, an unpaired two-tailed t-test was applied. If one or both datasets failed the normality test, a two-tailed Mann–Whitney U test was performed. Each parameter was analysed independently to compare the two CAF cell lines. Results were visualised using box and whisker plots displaying median and interquartile range. For the mean speed versus persistence analysis, correlation plots were generated separately for each cell line. Correlation coefficients were calculated using Spearman's rank correlation test.

Tail loss observation

To illustrate the tail loss phenomenon, a representative migrating VMC59F cell was selected from the time-lapse dataset in Fiji. The region of interest surrounding the selected cell was cropped for all relevant time points. Images corresponding to each time point were extracted to generate a sequential representation of the tail loss event. A scale bar was added to each image using the "Scale Bar" function under the "Analyze" tab to indicate spatial dimensions.

TGF-β1-treatment on Meso125F cells

Meso125F cells were seeded in 12-well plates and cultured under standard conditions. After cell attachment, cultures were either maintained in control medium or treated with recombinant TGF-β1 at a final working concentration of 5 ng/ml. Cells were cultured for a total of 7 days, and growth was assessed at defined time points on days 1, 4, and 7. Cell growth was evaluated by brightfield microscopy using a standard light microscope. At each time point, representative images of each well were acquired. The total covered area was analysed using Fiji. As overlapping cells were not segmented computationally, the analysis represents an approximation of overall cell growth rather than an exact quantification of individual cell numbers. The obtained values were compiled for descriptive comparison of growth dynamics between control and TGF-β1-treated cells.

ALD-R491-treatment of VMC59F

Cell seeding and drug-treatment for cell viability assay

VMC59F cells were seeded as described in Section *Cell Culture* in white 96-well plates at densities of 6,000 or 3,000 cells per well (100 µL total volume per well) and allowed to adhere overnight. The following day, cells were treated with the chemical component ALD-R491 at final concentrations of 5, 2.5, 1.25, 0.6, 0.3, and 0.15 µM. The drug ALD-R491 was dissolved in dimethyl sulfoxide (DMSO) and diluted in culture medium to achieve the desired final concentrations. Corresponding vehicle controls containing 0.2%, 0.1%, or 0.05% DMSO were included to match the DMSO concentration present at the respective drug concentrations. Wells containing cells without DMSO served as additional controls. Each condition was performed in technical duplicates. All remaining unused wells were filled with medium to minimise evaporation of wells containing a sample or control.

Cell viability assay

Cell viability was determined using the CellTiter-Glo® Luminescent Cell Viability Assay (Promega) according to the manufacturer's instructions. This assay quantifies intracellular adenosine triphosphate (ATP) levels as a surrogate marker for metabolically active and viable cells. The assay reagent induces cell lysis and generates a luminescent signal proportional to the amount of ATP present, which correlates with the number of viable cells. After 72 h of drug exposure, an equal volume of CellTiter-Glo reagent was added to each well. Plates were gently mixed to ensure complete cell lysis and incubated at room temperature for 30 min to stabilise the luminescent signal. Luminescence was measured using an EnVision multimode plate reader (PerkinElmer). Wells containing medium only were included to determine background luminescence.

Data analysis

Raw luminescence values (relative light units, RLU) were exported and analysed using Microsoft Excel and GraphPad. Background signal was determined from medium-only wells and subtracted from all measurements. For each condition, technical replicates were averaged. Viability was expressed as percentage relative to the corresponding DMSO vehicle control using the following formula:

$$\text{Viability (\%)} = 100 \times \frac{\text{mean RLU}_{sample}}{\text{mean RLU}_{vehi}}$$

Dose–response dot plots were generated by plotting normalised viability against the drug concentration.

Cell seeding and drug-treatment for immunofluorescence imaging

VMC59F cells were seeded as described in the section *Cell Culture* into two 6-well plates at a density of 25,000 cells per well in 3 mL complete culture medium and allowed to adhere overnight. Prior to seeding, two sterile, non-overlapping glass coverslips were placed into each well to allow subsequent immunofluorescence staining. On the following day, cells were treated with 5 µM ALD-R491. The compound was dissolved in DMSO and diluted in complete medium to the desired working concentration. Corresponding control wells

received vehicle only (0.2% DMSO in culture medium) to match the solvent concentration present in the treatment condition. Cells were incubated for 4 h at 37° C and 5% CO_2 before fixation.

Fixation, immunofluorescence staining of cells

Fixation of cells

Following treatment, cells were briefly examined microscopically, and culture medium was removed. Cells were washed with PBS and fixed for 15 min at 37° C using a pre-warmed fixation/permeabilisation solution containing 3.7% paraformaldehyde, 0.2% Triton X-100 and 0.1% glutaraldehyde. After fixation, coverslips were washed twice with PBS.

Immunofluorescence staining

For antibody incubation, coverslips were carefully removed and excess liquid was blotted from the edges using sterile tissue paper. Coverslips were then placed cell-sided down onto drops of antibody solution pipetted onto parafilm. Primary staining was performed using mouse anti-vimentin antibody (2.5 µg/mL in 0.1% bovine serum albumin (BSA) in PBS) for 1 h at room temperature. Coverslips were washed with PBS and subsequently incubated with rabbit anti-α-tubulin primary antibody under identical conditions. Secondary staining was performed for 1 h at room temperature in the dark using goat anti-mouse IgG (H+L) Alexa Fluor™ 488 (2 µg/mL in 0.1% BSA). In a final staining step, coverslips were incubated for 1 h at room temperature in the dark with a 0.1% BSA solution containing goat anti-rabbit IgG (H+L) Alexa Fluor™ 568 (2 µg/mL), Alexa Fluor™ 647 phalloidin (56 nM) and 4′,6-diamidino-2-phenylindole (DAPI) (1 µg/mL). After each staining step, coverslips were washed with PBS.

Mounting of cover slips

Following the final wash, coverslips were incubated in PBS for 20 min in the dark and briefly dipped in double-distilled water. Excess liquid was removed and coverslips were mounted onto glass microscope slides using 15 µL Mowiol mounting medium per slide. Coverslips were placed cell-side down and allowed to cure flat in the dark at 7° C.

Immunofluorescence imaging

Fixed and stained samples were imaged 24 h after mounting using a Zeiss CellObserver 7 microscope at 20× and 40× magnification. Images were acquired in the DAPI, Vimentin (Alexa Fluor™ 488), Tubulin (Alexa Fluor™ 568) and Actin (Alexa Fluor™ 647) channels. All images were saved as TIF files and used for subsequent digital image analysis.

Coherency analysis of cytoskeletal components

Immunofluorescence images were analysed using Fiji. For each condition (ALD-R491 treated and DMSO control), individual fluorescence channels (vimentin, α-tubulin, and actin) were analysed separately. Single cells were manually outlined using the "Freehand Selection" tool to generate individual regions of interest (ROIs). ROIs were stored in the ROI Manager to ensure consistent analysis of all channels within the same cell. Prior to analysis, background subtraction was performed using the "Subtract Background" function (rolling ball radius with standard settings) to reduce background fluorescence. Cytoskeletal organisation was quantified using the OrientationJ plugin (OrientationJ Measure function). For each ROI, the structure tensor was calculated, and the coherency value was extracted. Coherency values range from 0 (isotropic organisation with no preferred orientation) to 1 (highly aligned structures with strong directional organisation). For each cell, coherency values were determined individually for the vimentin, tubulin, and actin channels. The resulting values were exported from Fiji and compiled for subsequent statistical analysis.

Statistical analysis and data visualisation

Raw coherency data obtained from Fiji were analysed using GraphPad Prism 6.

For each cytoskeletal component (vimentin, tubulin, and actin), values were entered into separate columns using the "Column" data table format to compare ALD-R491-treated cells with DMSO controls. Normal distribution was assessed using the D'Agostino–Pearson omnibus normality test under "Column analyses". If both datasets passed the normality test, an unpaired two-tailed t-test was applied. If one or both datasets failed the normality test, a two-tailed Mann–Whitney U test was performed. Vimentin, tubulin and actin were analysed independently to determine potential effects of ALD-R491 treatment. Results were visualised using box and whisker plots displaying median and interquartile range.

Morphological analysis following ALD-R491 treatment

To evaluate the effect of ALD-R491 on cellular morphology, VMC59F cells were treated with ALD-R491 or DMSO control as described above and subsequently subjected to immunofluorescence staining. Morphological parameters were quantified using the Vimentin channel, as it provided the most comprehensive visualisation of the entire cell body and cytoplasmic extensions. Image analysis was performed using Fiji (ImageJ). For each condition, individual cells were manually outlined using the “Freehand Selection” tool. Based on these regions of interest (ROIs), the parameters cell area, aspect ratio, and circularity were measured using the “Measure” function under the “Analyze” tab. Only clearly distinguishable single cells were included in the analysis. All measurements were exported from Fiji and compiled for statistical evaluation.

Representation of immunofluorescence imaging

For visual representation of cytoskeletal organisation, one representative VMC59F cell per condition (ALD-R491-treated and DMSO control) was selected. For each condition, individual fluorescence channels were displayed separately (vimentin, tubulin, and actin), along with a merged image combining all three channels. Scale bars were added to all images using the “Scale Bar” function in Fiji to indicate spatial dimensions.

Results

Live cell imaging

Morphological characterisation

The morphological characteristics of Meso125F and VMC59F cells were compared based on cell area (µm²), aspect ratio, and circularity (Figure 1A–C). Meso125F cells exhibited a significantly larger cell area compared to VMC59F cells (Figure 1A). The distribution revealed a markedly higher median area and increased variability in Meso125F, whereas VMC59F cells were generally smaller and more homogeneous in size (****, $p < 0.0001$, Mann–Whitney U test). In contrast, no significant differences were observed in aspect ratio between the two cell lines (Figure 1B). Both Meso125F and VMC59F cells displayed comparable median values and largely overlapping distributions, indicating similar degrees of cellular elongation (ns, Mann–Whitney U test). Similarly, circularity values did not differ significantly between the groups (Figure 1C). Both cell lines showed broad distributions, reflecting morphological heterogeneity, but overall cell shape compactness was comparable (ns, Mann–Whitney U test).

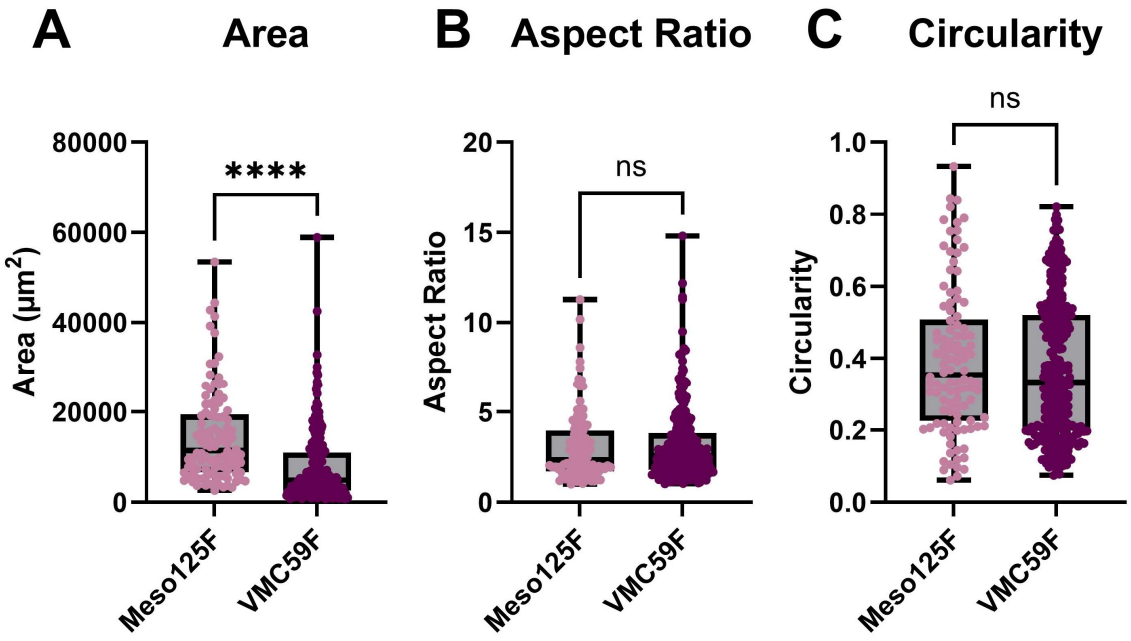

Figure 1: Morphological comparison of Meso125F and VMC59F cells. (A) Cell area distribution in µm². (B) Aspect ratio. (C) Circularity. Measurements for Meso125F (pink) and VMC59F (purple) shown as vertical dot and box plots displaying median and interquartile range with min–max whiskers. Statistical comparisons were performed using the Mann–Whitney U test. Highly significant (****), $p < 0.0001$. Not significant (ns).

To visually illustrate the morphological differences between the two CAF cell lines, representative phase-contrast images of a Meso125F cell and a VMC59F cell are shown (Figure 2). The images reflect the overall trend observed in the quantitative analysis, where Meso125F cells exhibited a larger cell area compared to VMC59F cells. The displayed cells were selected as representative examples approximating the average size difference observed between the two cell populations. It should be noted that the images serve purely illustrative purposes and do not represent the full variability of the analysed datasets.

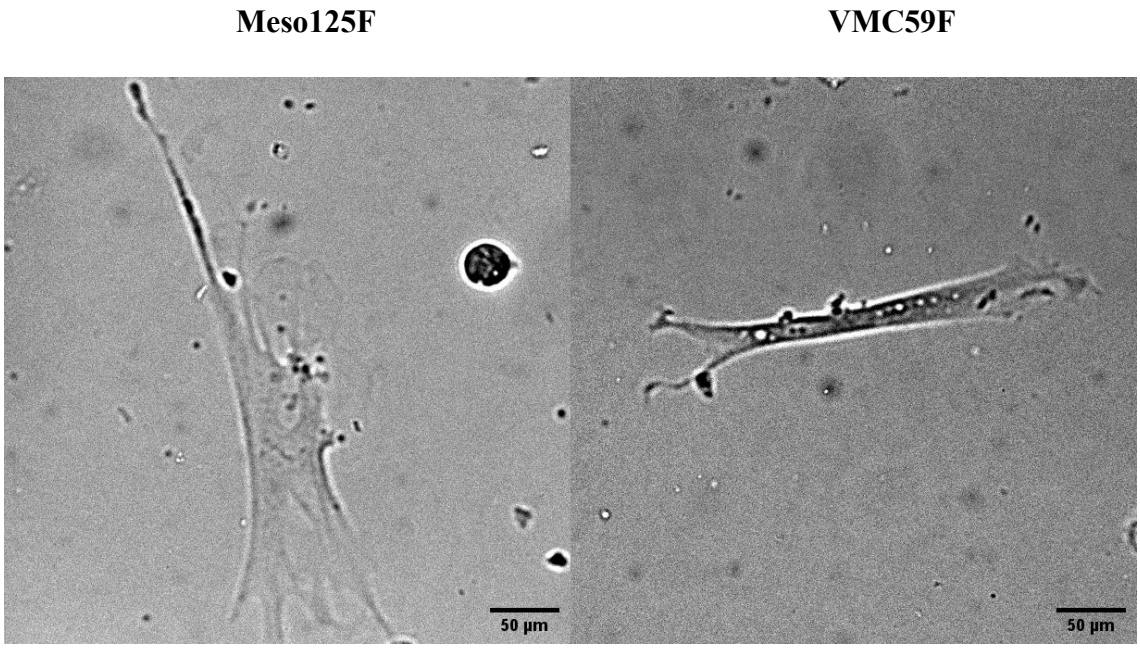

Figure 2: Representative phase contrast images of Meso125F and VMC59F cells. Meso125F on the left and VMC59F on the right image. Scale bar: 50 µm.

Migratory properties

The migratory behaviour of Meso125F and VMC59F cells was compared based on mean migration speed and persistence (Figure 3A, B). VMC59F cells exhibited a significantly higher mean migration speed compared to Meso125F cells (Figure 3A). The distribution revealed a markedly increased median speed in VMC59F, accompanied by greater variability, indicating enhanced heterogeneity in migration dynamics. Meso125F cells displayed consistently lower migration speeds. The difference between the two cell lines was highly significant (****, $p < 0.0001$, Mann–Whitney U test). In contrast to migration speed, persistence did not differ significantly between the two cell lines (Figure 3B). Both

Meso125F and VMC59F cells showed comparable median persistence values and largely overlapping distributions (ns, Mann–Whitney U test). The broad range of persistence values in both groups reflects heterogeneous migration patterns, with cells exhibiting both random and more directionally persistent movement.

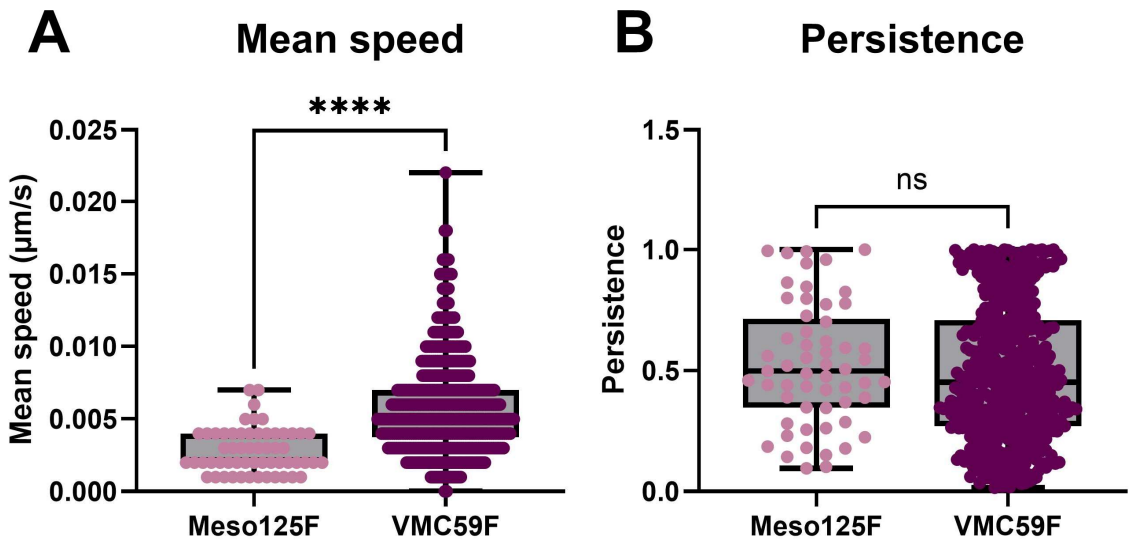

Figure 3: Migratory characteristics of Meso125F and VMC59F cells. (A) Distribution of mean migration speed. (B) Distribution of migration persistence. Measurements for Meso125F (pink) and VMC59F (purple) shown as vertical dot plots and box plots displaying median and interquartile range with min–max whiskers. Statistical comparisons were performed using the Mann–Whitney U test. Highly significant (****), $p < 0.0001$. Not significant (ns).

Speed-persistence relationship

To investigate whether migration speed and persistence are functionally linked within each CAF cell line, correlation analyses were performed (Figure 4). In Meso125F cells (A), Spearman correlation analysis revealed a weak positive association between mean migration speed and persistence; however, this correlation did not reach statistical significance ($r = 0.22$, $p = 0.10$). These findings indicate that, in Meso125F cells, higher migration speed is not significantly associated with increased directional persistence. In contrast, VMC59F cells (B) exhibited a weak but statistically highly significant positive correlation between mean migration speed and persistence ($r = 0.25$, $p < 0.0001$). This suggests that, within VMC59F cells, increased migration speed is associated with enhanced directional persistence, indicating a more coordinated migratory phenotype.

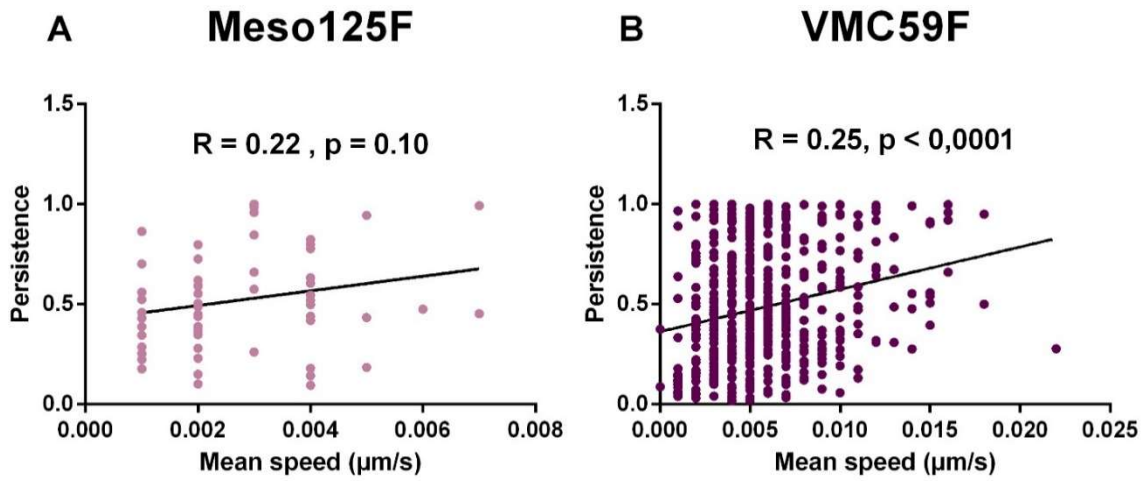

Figure 4: Correlation between migratory characteristics of Meso125F and VMC59F cells. Scatter plots show the relationship between mean speed and persistence for (A) Meso125F cells (pink) and (B) VMC59F cells (purple). Each dot represents a single cell. Meso125F (Spearman r = 0.22, p = 0.10) correlation and VMC59F (Spearman r = 0.25, p < 0.0001) correlation were assessed using Spearman's rank correlation test, and the linear regression line is shown.

Tail loss dynamics

A representative time-lapse sequence of a migrating VMC59F cell over a total duration of 280 minutes is shown (Figure 5). Images were acquired at 40-minute intervals to visualise dynamic morphological changes during cell migration. Over time, the cell exhibits progressive retraction of the trailing edge, culminating in a distinct tail loss event. Following detachment of the rear, the cell continues migration. These observations highlight the dynamic behaviour and rear-end remodelling characteristic of VMC59F cells.

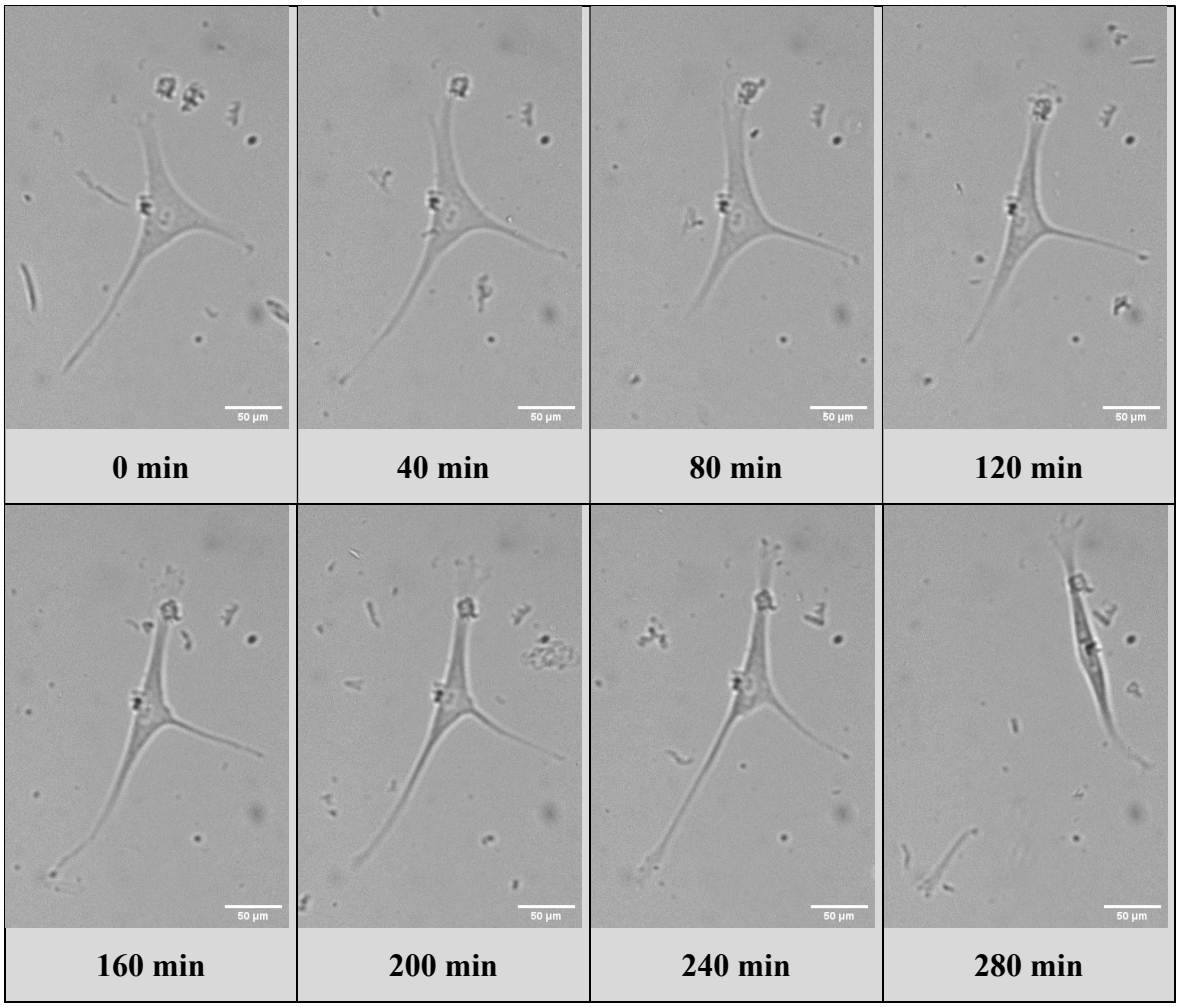

Figure 5: Representative time-lapse sequence of tail loss in a migrating VMC59F cell. Images were captured at 40-minute intervals over a total duration of 280 minutes. The sequence illustrates progressive rear retraction and a distinct tail loss event during migration. Scale bar: 50 µm.

Effect of TGF-β1 treatment on Meso125F cell growth

The time-dependent increase in total cell area of Meso125F cells under control conditions and TGF-β1 treatment was analysed over a period of 7 days (Figure 6).

In both groups, total cell area increased from day 1 to day 7, indicating progressive cell growth over time. However, TGF-β1-treated cells consistently exhibited lower total cell area compared to untreated controls at all analysed time points. While control cells showed a pronounced increase between day 1 and day 7, the increase observed in TGF-β1-treated cells appeared less prominent. It should be noted that the analysis is based on combined total cell area measurements and does not account for overlapping cells. Furthermore, no statistical

analysis was performed; therefore, the data provides a descriptive comparison rather than a quantitative statistical evaluation of growth differences.

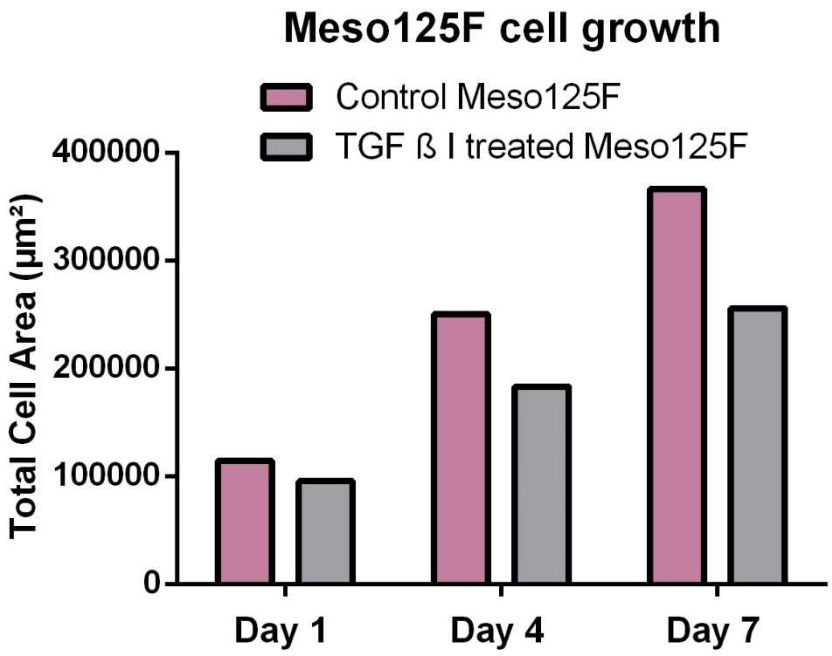

Figure 6: Total cell area comparison of untreated control and TGF-β1 treated Meso125F. The combined total cell area in μm^2 of the control Meso125F (pink) and the TGF-ß1 treated Meso125F (grey) on the y-axis over the analysed time period on the x-axis

ALD-R491 treatment of VMC59F cells

Effect of ALD-R491 on cell viability

To evaluate potential cytotoxic effects of ALD-R491, cell viability was assessed at increasing concentrations in VMC59F cells seeded at 6000 and 3000 cells per well (Figure 7).

Across the tested concentration range (0.15–5 µM), ALD-R491 did not reduce cell viability in either seeding density (Figure 7A, B). Instead, viability values remained close to or slightly above 100%, with no apparent dose-dependent decrease. Corresponding DMSO controls reflecting the solvent concentrations present in the respective ALD-R491 conditions were analysed in parallel (Figure 7C, D). Specifically, DMSO concentrations of 0.05 µM, 0.10 µM, and 0.20 µM corresponded to the solvent levels present in the 1.25 µM, 2.5 µM, and 5 µM ALD-R491 treatments, respectively. These solvent controls did not induce

substantial reductions in viability at either seeding density. These findings indicate that ALD-R491 does not exert cytotoxic effects under the tested conditions.

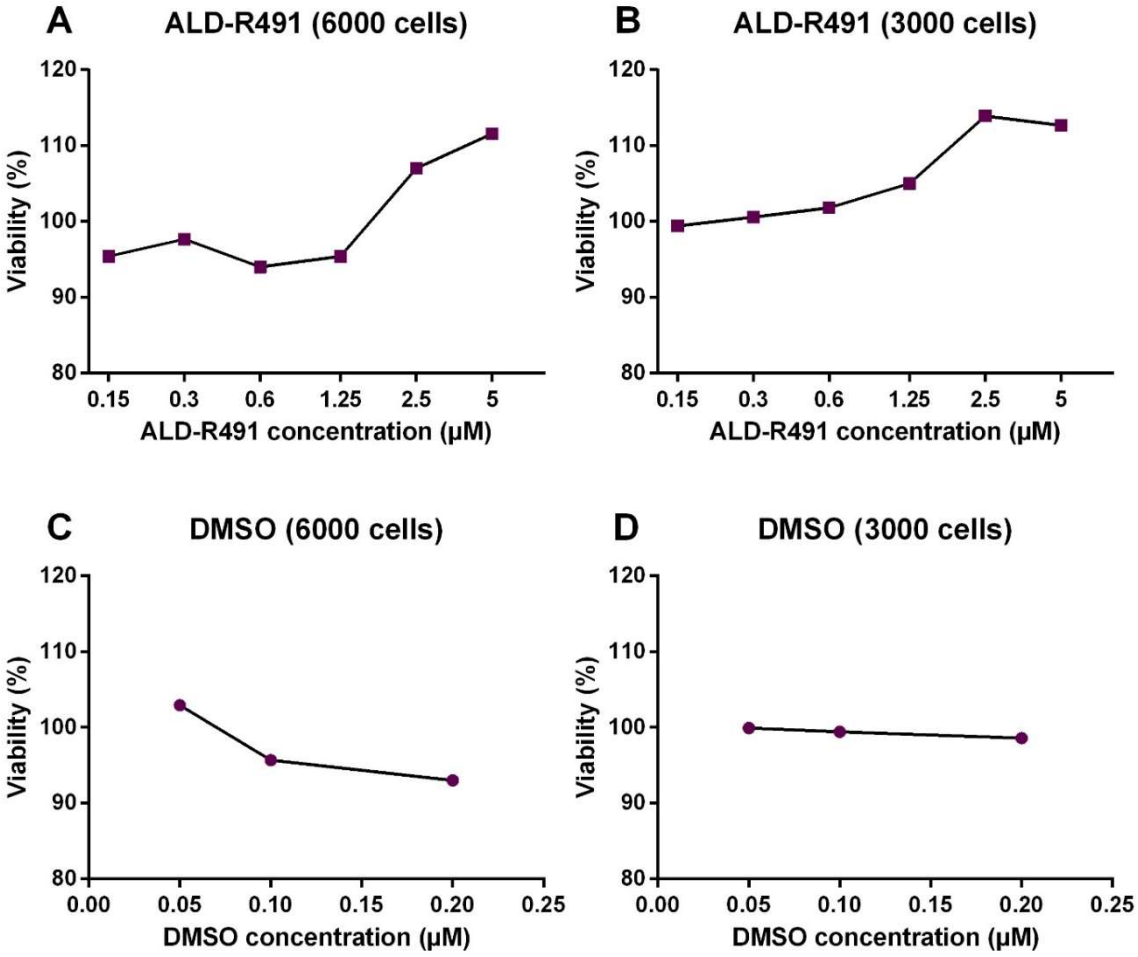

Figure 7: Effect of ALD-R491 on VMC59F cell viability. Cell viability was assessed following treatment with increasing concentrations of ALD-R491 at two seeding densities of VMC59F cells (A: 6000 cells; B: 3000 cells). Corresponding DMSO controls are shown in panels C (6000 cells) and D (3000 cells). DMSO concentrations of 0.05 µM, 0.10 µM, and 0.20 µM corresponded to the solvent levels present in the 1.25 µM, 2.5 µM, and 5 µM ALD-R491 treatments. Viability is expressed as percentage relative to untreated controls.

Effect of ALD-R491 on cell morphology of VMC59F cells

To assess whether ALD-R491 treatment alters cellular morphology, cell area, aspect ratio, and circularity were analysed following treatment and compared to DMSO controls (Figure 8).

ALD-R491 treatment resulted in a modest but statistically significant reduction in cell area compared to DMSO-treated cells (A, *p < 0.05, Mann–Whitney U test). In contrast, no

significant differences were observed in aspect ratio (B) or circularity (C), indicating that overall cell shape and elongation remained largely unaffected by ALD-R491 treatment (ns, Mann–Whitney U test). These findings suggest that while ALD-R491 may influence cell size, it does not induce pronounced morphological remodelling.

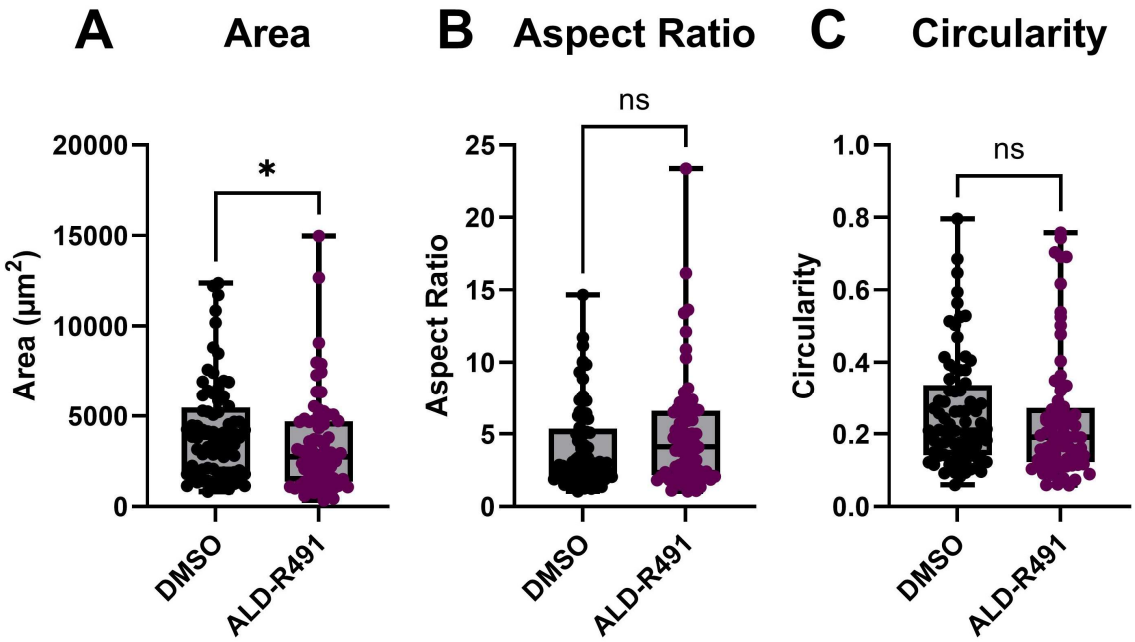

Figure 8: Effect of ALD-R491 on cell morphology with DMSO as control. (A) Cell area distribution in µm². (B) Aspect ratio. (C) Circularity. Measurements for DMSO control (black) and ALD-R491-treated (purple) shown as vertical dot and box plots displaying median and interquartile range with min–max whiskers. Statistical comparisons were performed using the Mann–Whitney U test. Significant (*), $p < 0.05$. Not significant (ns).

Effect of ALD-R491 on cytoskeletal organisation in VMC59F cells

To investigate whether ALD-R491 affects cytoskeletal organisation, coherency values were quantified for vimentin, tubulin, and actin filaments in VMC59F cells (Figure 9).

No significant differences in coherency were observed between ALD-R491-treated and DMSO-treated cells for any of the analysed cytoskeletal components (A–C). Vimentin organisation showed comparable median coherency values and overlapping distributions between treatment groups (A). Similarly, tubulin filament alignment did not differ significantly between ALD-R491 and control conditions (B). Actin coherency analysis also revealed no statistically significant differences between treated and untreated cells (C). Overall, these results indicate that short-term ALD-R491 treatment does not induce detectable alterations in global cytoskeletal filament alignment in VMC59F cells.

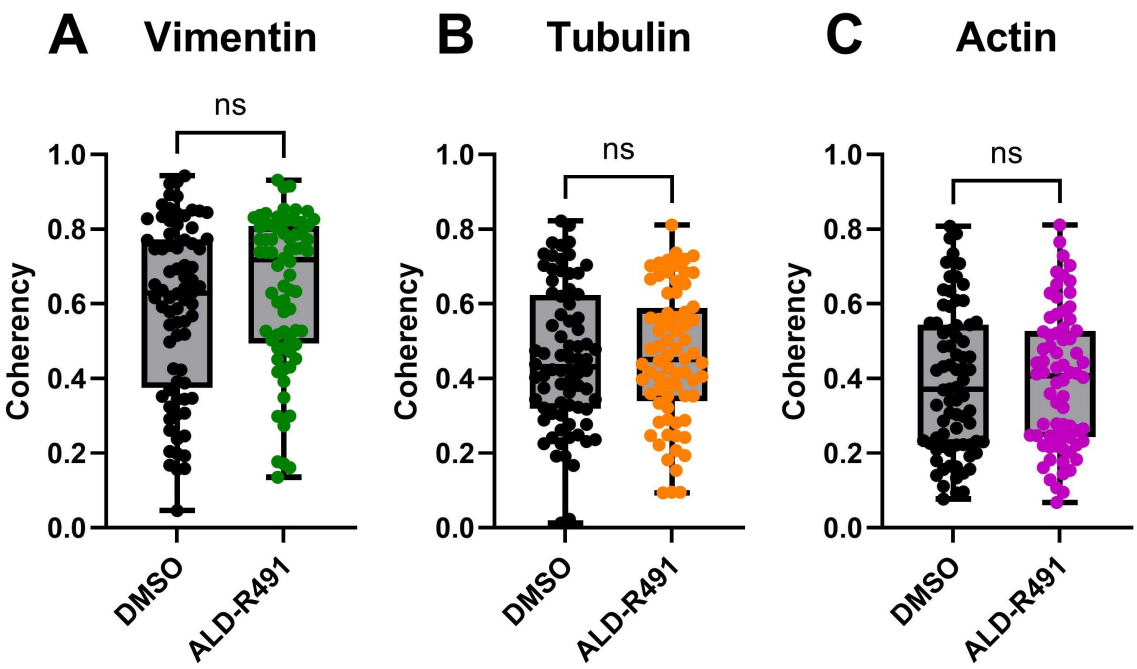

Figure 9: Quantification of cytoskeletal coherency in VMC59F cells following ALD-R491 treatment. (A) Vimentin (green), (B) tubulin (orange), and (C) actin (magenta) filament coherency values in ALD-R491- and DMSO-treated cells (black) shown as vertical dot plots and box plots displaying median and interquartile range with min–max whiskers. Statistical comparisons were performed using the Mann–Whitney test for vimentin and actin and the unpaired t-test for tubulin. Not significant (ns).

Representative immunofluorescence images of cytoskeletal organisation

Representative immunofluorescence images of VMC59F cells treated with DMSO or ALD-R491, stained for vimentin, α-tubulin, and actin with merged images shown in the rightmost column, are presented (Figure 10).

Consistent with the quantitative coherency analysis, no overt alterations in filament organisation, distribution, or overall cytoskeletal architecture were observed following ALD-R491 treatment. Vimentin intermediate filaments exhibited a typical filamentous network extending throughout the cytoplasm under both conditions. Tubulin staining revealed intact microtubule arrays radiating from the perinuclear region toward the cell periphery, without apparent disruption upon drug treatment. Actin filaments displayed characteristic stress fiber structures in both groups. Overall, qualitative inspection of representative cells corroborates the quantitative findings, indicating that short-term ALD-R491 treatment does not induce major structural rearrangements of the cytoskeleton in VMC59F cells.

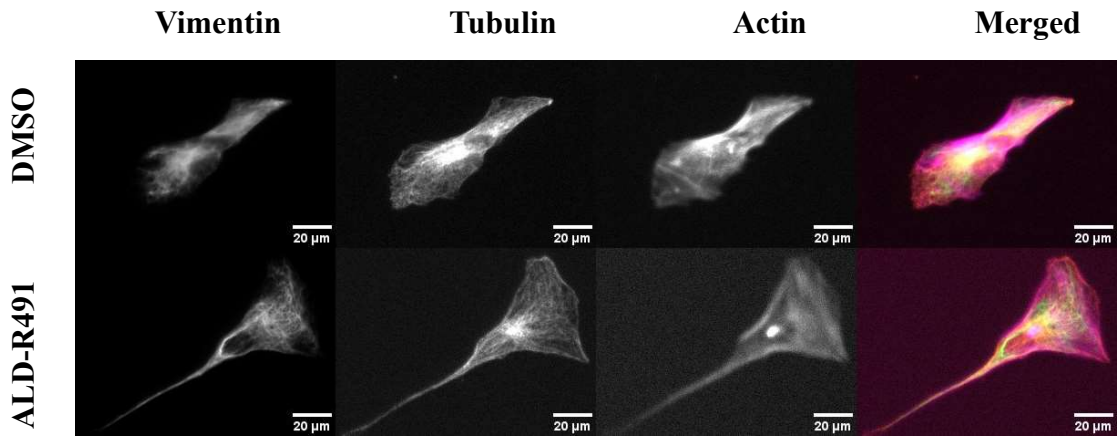

Figure 10: Representative immunofluorescence images of VMC59F cells treated with ALD-R491 or DMSO. Cells were stained for vimentin (left), α-tubulin (middle left), and actin (middle right) under DMSO-treated (top) control condition and ALD-R491-treated (bottom) condition. Merged images are shown in the rightmost column. Scale bar: 20 µm.

Discussion

CAF heterogeneity and patient-specific phenotypes

The present study sought to investigate whether cancer-associated fibroblasts derived from pleural mesothelioma patients with distinct clinical outcomes exhibit functional differences in morphology and migration behaviour.

A central finding of this study is the presence of marked phenotypic differences between Meso125F and VMC59F cells, which appear to reflect the clinical outcomes of the respective patients. CAFs derived from the Meso125F patient, who exhibited a substantially longer survival time (1028 days after diagnosis), displayed significantly larger cell areas and greater size variability, together with reduced migratory capacity. In contrast, VMC59F cells, originating from a patient with a shorter survival time (420 days after diagnosis), exhibited significantly higher mean migration speed and a more compact morphology. Notably, the survival time of the Meso125F patient was approximately 2.5-fold longer than that of the VMC59F patient, which is consistent with the observed differences in CAF phenotype. These findings suggest that patient-derived CAFs retain intrinsic, patient-specific functional characteristics in vitro, and may reflect differences in tumour aggressiveness.

Notably, migration persistence did not differ significantly between the two cell lines. However, correlation analysis revealed that in VMC59F cells, persistence increased in relation to migration speed, whereas no such association was observed in Meso125F cells. This suggests that VMC59F cells may exhibit a more coordinated migratory phenotype, in which increased speed is coupled to directional movement rather than random displacement.

Given that VMC59F was derived from a patient with more aggressive disease and shorter survival based on survival time after diagnosis, the observed increase in migration speed may reflect a stromal phenotype that potentially supports tumour progression. Although direct functional tumour–CAF interaction assays were not performed in this study, enhanced fibroblast motility could facilitate ECM remodelling, mechanical restructuring of the TME and tumour cell invasion. These findings are consistent with the concept that CAF populations are functionally heterogeneous and may differentially contribute to tumour aggressiveness. However, an important consideration concerns the stability of the CAF phenotype in vitro. CAFs are known to be highly plastic and dependent on signalling from tumour cells and the TME [20,51]. In prolonged monoculture conditions, CAFs may partially revert toward a more quiescent fibroblast phenotype and lose activation markers or

alter contractility and change migratory behaviour [20,51]. If such phenotypic drift occurred during cell culture, it could influence the interpretation of the results. For example, reduced activation might mask differences in cytoskeletal organisation or drug responsiveness. A more comprehensive characterisation of the CAF phenotype would therefore have strengthened the study. Analyses such as α-smooth muscle actin (α-SMA), fibroblast activation protein (FAP), fibronectin or collagen expression, transcriptomic profiling and comparison to normal fibroblasts could help assessing the genetic and activation status of the cells to clarify whether observed differences reflect intrinsic patient-specific programs or culture-adapted phenotypes [20,51].

Cytoskeletal organisation and vimentin targeting

Coherency analysis of vimentin, tubulin and actin revealed no significant differences between ALD-R491-treated and control VMC59F cells. Furthermore, ALD-R491 did not induce marked changes in cell elongation or circularity. Interestingly, ALD-R491 treatment resulted in a modest but statistically significant reduction in cell area without affecting overall cell shape parameters. This suggests that vimentin targeting may influence aspects of cytoskeletal tension or cell spreading without inducing large-scale structural rearrangements detectable by global coherency measurements. It is important to consider that coherency analysis quantifies global filament alignment but does not capture local filament rearrangements, network dynamics or post-translational modifications. Therefore, subtle alterations in filament organisation or mechanical properties may not be reflected in the performed analysis. Additionally, live cell imaging following ALD-R491 treatment could have provided highly valuable information. Given that vimentin contributes to cellular mechanics and migratory behaviour, dynamic parameters like migration speed, directional persistence, rear retraction efficiency or frequency of tail loss events may be more sensitive to vimentin modulation than static morphology. Since VMC59F cells exhibited a pronounced migratory phenotype, it would be particularly interesting to determine whether ALD-R491 reduces migration speed or alters speed–persistence coupling. Thus, live cell imaging under drug treatment conditions represents a logical and promising extension of the present work. It is therefore possible that ALD-R491 induces structural or mechanical alterations not detectable by global orientation metrics.

Overall, the data suggest that under the tested conditions, ALD-R491 does not cause overt cytoskeletal disruption in mesothelioma-derived CAFs. This is in line with the viability

assay, which demonstrated no reduction in metabolic activity across tested concentrations. Notably, a slight increase in viability was observed with increasing ALD-R491 concentrations, with values reaching up to approximately 110%, suggesting a potential stimulatory or protective effect on cellular metabolism. This observation is particularly interesting given that in preclinical models, ALD-R491 has been shown to influence mesenchymal cell behaviour, partially reverse epithelial-to-mesenchymal transition phenotypes, and exert anti-inflammatory and host-protective effects. Together, these findings indicate that ALD-R491 does not induce acute cytotoxicity and that its biological effects may be modulatory, context-dependent, or require longer exposure times.

TGF-β1-mediated growth modulation

Throughout the experimental period, Meso125F cells consistently exhibited slower growth and reduced expansion compared to VMC59F cells, which increasingly limited the feasibility of performing parallel experiments and direct comparisons between the two cell lines. To address this, TGF-β1 treatment was applied with the aim of enhancing proliferation and potentially restoring or maintaining a more activated CAF phenotype in Meso125F cells.

TGF-β1 stimulation resulted in progressive increases in total cell area over time in both treated and untreated conditions, reflecting ongoing cell growth. Interestingly, TGF-β1-treated cells consistently exhibited lower total cell area compared to controls. Although no statistical testing was performed and the analysis does not account for overlapping cells, this observation suggests that TGF-β1 may influence growth dynamics in a context-dependent manner. TGF-β1 is widely recognised as a key regulator of fibroblast activation and myofibroblast differentiation. However, its effects can vary depending on cellular state, confluency, and microenvironmental conditions. In this context, the lack of a clear growth-promoting effect may indicate that Meso125F cells respond differently to canonical activation cues, or that their reduced proliferative capacity cannot be readily rescued by TGF-β1 alone. The present findings highlight the complexity of CAF responses to activation signals and underscore the need for more detailed quantitative proliferation and activation marker analyses in future studies.

Tail loss and migratory dynamics

The representative tail loss sequence illustrates dynamic rear-end retraction during migration, emphasising the active cytoskeletal remodelling capacity of VMC59F cells. Although tail loss was analysed qualitatively, the visualisation supports the concept that these CAFs undergo substantial cytoskeletal tension release and adhesion disassembly events during movement. Future studies incorporating quantitative rear-detachment metrics or focal adhesion analyses would allow deeper mechanistic insight into the migratory phenotype differences observed between the two cell lines.

Limitations

Several limitations should be acknowledged. First, the study is based on two CAF cell lines, which limits generalisability. CAF populations are known to exhibit extensive inter- and intra-tumoural heterogeneity [20,51], and additional patient-derived lines would strengthen the robustness of the conclusions. Second, some analyses, such as TGF-β1-mediated growth assessment and tail loss quantification, were descriptive in nature and not statistically powered. Third, coherency analysis provides a global structural overview but does not capture fine-scale cytoskeletal dynamics.

In addition, although DAPI nuclear staining was performed during immunofluorescence imaging, nuclear images were not included in the final analysis due to suboptimal staining quality. The likely cause was insufficient equilibration of the DAPI solution to room temperature prior to application, potentially leading to crystal formation and reduced staining efficiency. While this technical limitation did not affect cytoskeletal coherency or morphology measurements derived from the vimentin channel, improved nuclear visualisation would have facilitated more precise segmentation and potentially supported automated quantitative analyses.

Furthermore, no direct functional assays linking CAF behaviour to tumour cell invasion, matrix remodelling, or mechanical force generation were performed. Therefore, conclusions regarding clinical relevance remain indirect and hypothesis-generating rather than mechanistically confirmed.

Future perspectives

Future investigations should expand this work by incorporating additional CAF lines derived from patients with diverse clinical outcomes to better capture inter-patient heterogeneity and strengthen the generalisability of the findings. Functional co-culture assays with mesothelioma cells would allow direct assessment of how CAF phenotypes influence tumour cell behaviour, including proliferation, invasion, and therapy response. Furthermore, extended treatment experiments with ALD-R491, combined with live-cell imaging approaches, would provide deeper insight into the temporal dynamics of cytoskeletal modulation and migratory behaviour. Complementary analyses of CAF activation markers, such as α-SMA, fibronectin, and FAP, as well as transcriptomic or proteomic profiling, could help to define phenotypic states and assess their stability in vitro. In addition, quantification of extracellular matrix (ECM) remodelling capacity and the application of traction force microscopy would enable a more comprehensive evaluation of CAF-mediated mechanical properties and contractility. Collectively, these approaches would provide more detailed mechanistic insight into how CAF phenotypes contribute to tumour progression and help to clarify whether targeting vimentin represents a viable strategy for stromal modulation in pleural mesothelioma.

Conclusion

This work aimed to comparatively characterise morphology, migration behaviour and drug responsiveness of CAFs derived from PM patients with distinct clinical outcomes. By integrating quantitative live cell imaging, cytoskeletal organisation analysis and pharmacological modulation experiments, the present work provides functional evidence for CAF heterogeneity at both morphological and migratory levels.

At baseline, the two CAF cell lines displayed clear phenotypic differences. Meso125F cells exhibited significantly larger cell areas and greater variability in size, whereas VMC59F cells demonstrated markedly higher mean migration speed. In contrast, aspect ratio, circularity and migration persistence did not differ significantly between the two cell lines. Importantly, correlation analysis revealed that migration speed and persistence were positively associated in VMC59F cells but not in Meso125F cells, suggesting a more coordinated migratory phenotype in VMC59F. These findings suggest that CAFs derived from patients with longer survival times exhibit larger cell areas and lower mean migration speeds, whereas CAFs derived from patients with shorter survival times display smaller cell areas and higher mean migration speeds.

Stimulation with TGF-β1 resulted in progressive cell growth over time in Meso125F cells under both treated and untreated conditions. Although TGF-β1-treated cells exhibited consistently lower total cell area compared to controls, the analysis was descriptive in nature and did not include statistical testing. These observations nevertheless suggest context-dependent effects of TGF-β1 on CAF growth dynamics.

Pharmacological targeting of vimentin using ALD-R491 did not impair cell viability at the tested concentrations. While ALD-R491 treatment induced a modest but statistically significant reduction in cell area, no significant changes were observed in aspect ratio, circularity or cytoskeletal coherency of vimentin, tubulin or actin filaments. Thus, ALD-R491 did not cause pronounced global cytoskeletal reorganisation under the investigated conditions, indicating that its effects on CAF biology may be subtle and not necessarily reflected by large-scale structural alterations.

Collectively, these findings demonstrate that CAFs derived from pleural mesothelioma patients with different clinical outcomes exhibit distinct morphological and migratory phenotypes. Moreover, the data suggest that pharmacological modulation of vimentin does not induce overt cytoskeletal restructuring but may influence specific aspects of cell

behaviour. This work highlights the functional heterogeneity of mesothelioma-associated fibroblasts and underscores the importance of considering stromal diversity when investigating TME dynamics and therapeutic targeting strategies.

References

1. Bertuccio FR, Montini S, Fusco MA, Gennaro AD, Sciandrone G, Agustoni F, et al. Malignant Pleural Mesothelioma: From Pathophysiology to Innovative Actionable Targets. Cancers. 2025;17. doi:10.3390/cancers17071160

2. Jain M, Crites MK, Rich P, Bajantri B. Malignant Pleural Mesothelioma: A Comprehensive Review. J Clin Med. 2024;13:5837. doi:10.3390/jcm13195837 PubMed PMID: 39407894; PubMed Central PMCID: PMC11476893.

3. Fu L, Liu K, Liu Y, Gao Y, Wang B, Sun Y, et al. Global patterns and trends in mesothelioma incidence: A retrospective cross-sectional study. Lung Cancer. 2026;211:108878. doi:10.1016/j.lungcan.2025.108878

4. Ronsmans S, Nackaerts K, Nemery B. Update on mesothelioma incidence and forecast of future cases in Belgium. BMC Public Health. 2025;25:3870. doi:10.1186/s12889-025-25212-8

5. Congedo MT, West EC, Evangelista J, Mattingly AA, Calabrese G, Sassorossi C, et al. The genetic susceptibility in the development of malignant pleural mesothelioma: somatic and germline variants, clinicopathological features and implication in practical medical/surgical care: a narrative review. J Thorac Dis. 2024;16:671–87. doi:10.21037/jtd-23-611 PubMed PMID: 38410609; PubMed Central PMCID: PMC10894363.

6. Klampatsa A, Albelda SM. Current Advances in CAR T Cell Therapy for Malignant Mesothelioma. J Cell Immunol. 2020;Volume 2:192–200. doi:10.33696/immunology.2.042

7. Brcic L, Kern I. Clinical significance of histologic subtyping of malignant pleural mesothelioma. Transl Lung Cancer Res. 2020;9:924–33. doi:10.21037/tlcr.2020.03.38 PubMed PMID: 32676358; PubMed Central PMCID: PMC7354152.

8. Ries A, Flehberger D, Slany A, Pirker C, Mader JC, Mohr T, et al. Mesothelioma-associated fibroblasts enhance proliferation and migration of pleural mesothelioma cells via c-Met/PI3K and WNT signaling but do not protect against cisplatin. J Exp Clin

Cancer Res. 2023;42:27. doi:10.1186/s13046-022-02582-0 PubMed PMID: 36683050; PubMed Central PMCID: PMC9869633.

9. Cedres S, Valdivia A, Priano I, Rocha P, Iranzo P, Pardo N, et al. BAP1 Mutations and Pleural Mesothelioma: Genetic Insights, Clinical Implications, and Therapeutic Perspectives. Cancers. 2025;17. doi:10.3390/cancers17091581

10. Hiltbrunner S, Fleischmann Z, Sokol ES, Zoche M, Felley-Bosco E, Curioni-Fontecedro A. Genomic landscape of pleural and peritoneal mesothelioma tumours. Br J Cancer. 2022;127:1997–2005. doi:10.1038/s41416-022-01979-0 PubMed PMID: 36138075; PubMed Central PMCID: PMC9681755.

11. Imai H. Current drug therapy for pleural mesothelioma. Respiratory Investigation. 2025;63:200–9. doi:10.1016/j.resinv.2024.12.017

12. Menis J, Pasello G, Remon J. Immunotherapy in malignant pleural mesothelioma: a review of literature data. Transl Lung Cancer Res. 2021;10:2988–3000. doi:10.21037/tlcr-20-673 PubMed PMID: 34295692; PubMed Central PMCID: PMC8264322.

13. Almazrouei KM, Mishra V, Pandya H, Sambhav K, Bhavsar SN. Tumor Microenvironment and Its Role in Cancer Progression: An Integrative Review. Cureus. 2025;17:e92707. doi:10.7759/cureus.92707 PubMed PMID: 41116947.

14. Fathah D e, Ejaz S. Role of tumor microenvironment in cancer promotion, development of drug resistance and cancer treatment. J Egypt Natl Canc Inst. 2025;37:59. doi:10.1186/s43046-025-00317-8

15. Klampatsa A, O'Brien SM, Thompson JC, Rao AS, Stadanlick JE, Martinez MC, et al. Phenotypic and functional analysis of malignant mesothelioma tumor-infiltrating lymphocytes. OncoImmunology. 2019;8:e1638211. doi:10.1080/2162402X.2019.1638211 PubMed PMID: 31428531.

16. Désage AL, Karpathiou G, Peoc'h M, Froudarakis ME. The Immune Microenvironment of Malignant Pleural Mesothelioma: A Literature Review. Cancers (Basel). 2021;13:3205. doi:10.3390/cancers13133205 PubMed PMID: 34206956; PubMed Central PMCID: PMC8269097.

17. Sahai E, Astsaturov I, Cukierman E, DeNardo DG, Egeblad M, Evans RM, et al. A framework for advancing our understanding of cancer-associated fibroblasts. Nat Rev Cancer. 2020;20:174–86. doi:10.1038/s41568-019-0238-1

18. Guo T, Xu J. Cancer-associated fibroblasts: a versatile mediator in tumor progression, metastasis, and targeted therapy. Cancer Metastasis Rev. 2024;43:1095–116. doi:10.1007/s10555-024-10186-7 PubMed PMID: 38602594; PubMed Central PMCID: PMC11300527.

19. Chen Y, McAndrews KM, Kalluri R. Clinical and therapeutic relevance of cancer-associated fibroblasts. Nat Rev Clin Oncol. 2021;18:792–804. doi:10.1038/s41571-021-00546-5 PubMed PMID: 34489603; PubMed Central PMCID: PMC8791784.

20. Yang D, Liu J, Qian H, Zhuang Q. Cancer-associated fibroblasts: from basic science to anticancer therapy. Exp Mol Med. 2023;55:1322–32. doi:10.1038/s12276-023-01013-0

21. Erdogan B, Webb DJ. Cancer-associated fibroblasts modulate growth factor signaling and extracellular matrix remodeling to regulate tumor metastasis. Biochem Soc Trans. 2017;45:229–36. doi:10.1042/BST20160387 PubMed PMID: 28202677; PubMed Central PMCID: PMC5371349.

22. Louault K, Li RR, DeClerck YA. Cancer-Associated Fibroblasts: Understanding Their Heterogeneity. Cancers (Basel). 2020;12:3108. doi:10.3390/cancers12113108 PubMed PMID: 33114328; PubMed Central PMCID: PMC7690906.

23. Lynch MD, Watt FM. Fibroblast heterogeneity: implications for human disease. J Clin Invest. 128:26–35. doi:10.1172/JCI93555 PubMed PMID: 29293096; PubMed Central PMCID: PMC5749540.

24. Parker JB, Valencia C, Akras D, DiIorio SE, Griffin MF, Longaker MT, et al. Understanding Fibroblast Heterogeneity in Form and Function. Biomedicines. 2023;11. doi:10.3390/biomedicines11082264

25. Patteson AE, Carroll RJ, Iwamoto DV, Janmey PA. The vimentin cytoskeleton: When polymer physics meets cell biology. Phys Biol. 2020;18:011001. doi:10.1088/1478-3975/abbcc2 PubMed PMID: 32992303; PubMed Central PMCID: PMC8240483.

26. Hohmann T, Dehghani F. The Cytoskeleton—A Complex Interacting Meshwork. Cells. 2019;8:362. doi:10.3390/cells8040362 PubMed PMID: 31003495; PubMed Central PMCID: PMC6523135.

27. Conboy JP, Istúriz Petitjean I, van der Net A, Koenderink GH. How cytoskeletal crosstalk makes cells move: Bridging cell-free and cell studies. Biophys Rev (Melville). 2024;5:021307. doi:10.1063/5.0198119 PubMed PMID: 38840976; PubMed Central PMCID: PMC11151447.

28. Seetharaman S, Etienne-Manneville S. Cytoskeletal Crosstalk in Cell Migration. Trends in Cell Biology. 2020;30:720–35. doi:10.1016/j.tcb.2020.06.004

29. Alonso-Matilla R, Provenzano PP, Odde DJ. Physical principles and mechanisms of cell migration. npj Biol Phys Mech. 2025;2:2. doi:10.1038/s44341-024-00008-w

30. Chang Y, Lee JWN, Holle AW. The mechanobiology of fibroblast activation in disease. APL Bioeng. 2025;9:021505. doi:10.1063/5.0272393 PubMed PMID: 40538750; PubMed Central PMCID: PMC12178607.

31. Liao CY, Hundscheid JHM, Crawford J, ten Dijke P, Coornaert B, Danen EHJ. Novel high throughput 3D ECM remodeling assay identifies MEK as key driver of fibrotic fibroblast activity. Materials Today Bio. 2025;32:101800. doi:10.1016/j.mtbio.2025.101800

32. Garcin C, Straube A. Microtubules in cell migration. Essays Biochem. 2019;63:509–20. doi:10.1042/EBC20190016 PubMed PMID: 31358621; PubMed Central PMCID: PMC6823166.

33. Nayak P, Dasanna AK, Paul R, Rieger H. Modeling actin-microtubule crosstalk in migrating cells. Biophysical Journal. 2025;124:3742–54. doi:10.1016/j.bpj.2025.09.029 PubMed PMID: 40993997.

34. Gorelik R, Gautreau A. Quantitative and unbiased analysis of directional persistence in cell migration. Nat Protoc. 2014;9:1931–43. doi:10.1038/nprot.2014.131 PubMed PMID: 25033209.

35. Hu Y, Becker ML, Willits RK. Quantification of cell migration: metrics selection to model application. Front Cell Dev Biol. 2023;11. doi:10.3389/fcell.2023.1155882

36. Liu J, Liu Z, Chen K, Chen W, Fang X, Li M, et al. Kindlin-2 promotes rear focal adhesion disassembly and directional persistence during cell migration. J Cell Sci. 2021;134:jcs244616. doi:10.1242/jcs.244616

37. Kirfel G, Rigort A, Borm B, Herzog V. Cell migration: mechanisms of rear detachment and the formation of migration tracks. European Journal of Cell Biology. 2004;83:717–24. doi:10.1078/0171-9335-00421

38. Barnes JL, Gorin Y. Myofibroblast Differentiation During Fibrosis: Role of NAD(P)H Oxidases. Kidney Int. 2011;79:944–56. doi:10.1038/ki.2010.516 PubMed PMID: 21307839; PubMed Central PMCID: PMC3675765.

39. Carthy JM. TGFβ signaling and the control of myofibroblast differentiation: Implications for chronic inflammatory disorders. Journal of Cellular Physiology. 2018;233:98–106. doi:10.1002/jcp.25879

40. Melchionna R, Trono P, Tocci A, Nisticò P. Actin Cytoskeleton and Regulation of TGFβ Signaling: Exploring Their Links. Biomolecules. 2021;11. doi:10.3390/biom11020336

41. Deng Z, Fan T, Xiao C, Tian H, Zheng Y, Li C, et al. TGF-β signaling in health, disease and therapeutics. Sig Transduct Target Ther. 2024;9:61. doi:10.1038/s41392-024-01764-w

42. Grauel AL, Nguyen B, Ruddy D, Laszewski T, Schwartz S, Chang J, et al. TGFβ-blockade uncovers stromal plasticity in tumors by revealing the existence of a subset of interferon-licensed fibroblasts. Nat Commun. 2020;11:6315. doi:10.1038/s41467-020-19920-5 PubMed PMID: 33298926; PubMed Central PMCID: PMC7725805.

43. Nicolini F, Bocchini M, Bronte G, Delmonte A, Guidoboni M, Crinò L, et al. Malignant Pleural Mesothelioma: State-of-the-Art on Current Therapies and Promises for the Future. Front Oncol. 2020;9:1519. doi:10.3389/fonc.2019.01519 PubMed PMID: 32039010; PubMed Central PMCID: PMC6992646.

44. Borea F, Franczak MA, Garcia M, Perrino M, Cordua N, Smolenski RT, et al. Target Therapy in Malignant Pleural Mesothelioma: Hope or Mirage? Int J Mol Sci. 2023;24:9165. doi:10.3390/ijms24119165 PubMed PMID: 37298116; PubMed Central PMCID: PMC10253134.

45. Tedesco J, Jaradeh M, Vigneswaran WT. Malignant Pleural Mesothelioma: Current Understanding of the Immune Microenvironment and Treatments of a Rare Disease. Cancers (Basel). 2022;14:4415. doi:10.3390/cancers14184415 PubMed PMID: 36139575; PubMed Central PMCID: PMC9496741.

46. Cao Z, Quazi S, Arora S, Osellame LD, Burvenich IJ, Janes PW, et al. Cancer-associated fibroblasts as therapeutic targets for cancer: advances, challenges, and future prospects. J Biomed Sci. 2025;32:7. doi:10.1186/s12929-024-01099-2

47. Kim HR, Warrington SJ, López-Guajardo A, Al Hennawi K, Cook SL, Griffith ZDJ, et al. ALD-R491 regulates vimentin filament stability and solubility, cell contractile force, cell migration speed and directionality. Front Cell Dev Biol. 2022;10:926283. doi:10.3389/fcell.2022.926283 PubMed PMID: 36483676; PubMed Central PMCID: PMC9723350.

48. Wu J, Wang S, Yu K, Xu Z, Wu X, Symmes D, et al. Oral Treatment with the Vimentin-Targeting Compound ALD-R491 Mitigates Hyperinflammation, Multi-Organ Injury, and Mortality in CLP-Induced Septic Mice. Life (Basel). 2025;15:1563. doi:10.3390/life15101563 PubMed PMID: 41157235; PubMed Central PMCID: PMC12565683.

49. Rosier M, Krstulović A, Kim HR, Kaur N, Enakireru EM, Symmes D, et al. The Vimentin-Targeting Drug ALD-R491 Partially Reverts the Epithelial-to-Mesenchymal Transition and Vimentin Interactome of Lung Cancer Cells. Cancers (Basel). 2024;17:81. doi:10.3390/cancers17010081 PubMed PMID: 39796712; PubMed Central PMCID: PMC11720119.

50. Hou SY, Macfarlane SC, Gómez Torijano A, Kim HR, Rosier M, Dobra K, et al. Cancer-Associated Fibroblasts Move and Interact More with Triple-Negative Breast Cancer Cells and Stimulate Their Proliferation in a Hyaluronan-Dependent Manner. Cells. 2025;14:1663. doi:10.3390/cells14211663 PubMed PMID: 41227309; PubMed Central PMCID: PMC12606758.

51. Xia Z, De Wever O. The plasticity of cancer-associated fibroblasts. Trends in Cancer. 2025;11:770–89. doi:10.1016/j.trecan.2025.04.012

Acknowledgements

I would like to thank Katalin Dobra and Annica Gad for providing me with the opportunity to carry out my master's thesis at Karolinska Institutet.

I am especially grateful to Hanna Krynska but also Malihe Behzadi for their support, helpful discussions, and willingness to share their knowledge during my time in the lab as well as assisting me with conducting my experiments and data analysis.

Furthermore, I am very thankful to Florian Salomons from the Biomedicum Imaging Core Facility of Karolinska Institutet for his outstanding technical support. His assistance with microscopy setups, troubleshooting, and image acquisition was invaluable for this project.

AI Usage Statement

AI-based language tools were used to assist in the revision and linguistic refinement of selected text passages. All scientific content, including data analysis, interpretation, and all figures, were independently created by the author.